Single Atom Platinum Catalyst Construction Based on Graphene Defects

Xiaopeng Song[a,b‡], Jie Liu[a‡], Junjie Chen[a] and Xing Liu[a*]

a. Shanghai Key Laboratory of Atomic Control and Application of Inorganic 2D Supermaterials, Shanghai Applied Radiation Institute, Shanghai University, Shanghai 200444, China.

b. Shanghai Tongyuan Cheng Technology Co., Ltd, Shanghai 200237, China.

*Corresponding author E-mail: Xing Liu (liuxing0215@shu.edu.cn)

‡ These authors contributed equally to this work.

PS1: Computational Methods

The B3LYP method in the framework of DFT, which has been widely used in the studies of atoms and water molecules on solid surfaces[1-6], is used to study the intermolecular interactions. We employed the double-ζ basis to geometry optimizations, and a d-polarization function is added (marked with 6-31G(d)) for the carbon, hydrogen and oxygen atoms. At the same time, the pseudopotential function with SDD[7] is introduced into the basis set for the Pt atom. A two-dimensional graphite surface with 66 carbon atoms and 20 passivated hydrogen atoms is used for the DFT study as shown in Figure. 1a, which is large enough to obtain results with a tolerable error, whereas the detailed discussions are shown in our former article[8-18]. All calculations are carried out using the Gaussian-16 package[19]. Before evaluating Pt adsorption, the formation energies of the defective graphene models were first calculated to assess their relative thermodynamic stability. The defect formation energy was defined as $E_f = E_{defect} - E_{pristine}$, where E_{defect} and $E_{pristine}$ are the total energies of the defective and pristine graphene models, respectively. Since all defective models considered in this work have the same atomic composition as the pristine graphene cluster, this definition directly reflects the energy cost associated with defect reconstruction. The adsorption energy of the Pt atom on graphene defects is calculated as $E_{ads}=E_{Pt@gra}-E_{Pt}-E_{gra}$, where the $E_{Pt@gra}$, E_{Pt} and E_{gra} are the total energies of the Pt atom with defected graphene, the Pt atom and the defected graphene, respectively.

PS2：The effect of graphene cluster size

To evaluate whether the finite graphene cluster used in this work can reasonably represent the local environment of a graphene-supported Pt site, an additional larger cluster model ($C_{84}H_{24}$) was constructed and compared with the original $C_{66}H_{20}$ model. Representative 4-C and 8-C defect structures were selected for this comparison, and the corresponding geometric and electronic descriptors are summarized in Fig. S1 and Table S1.

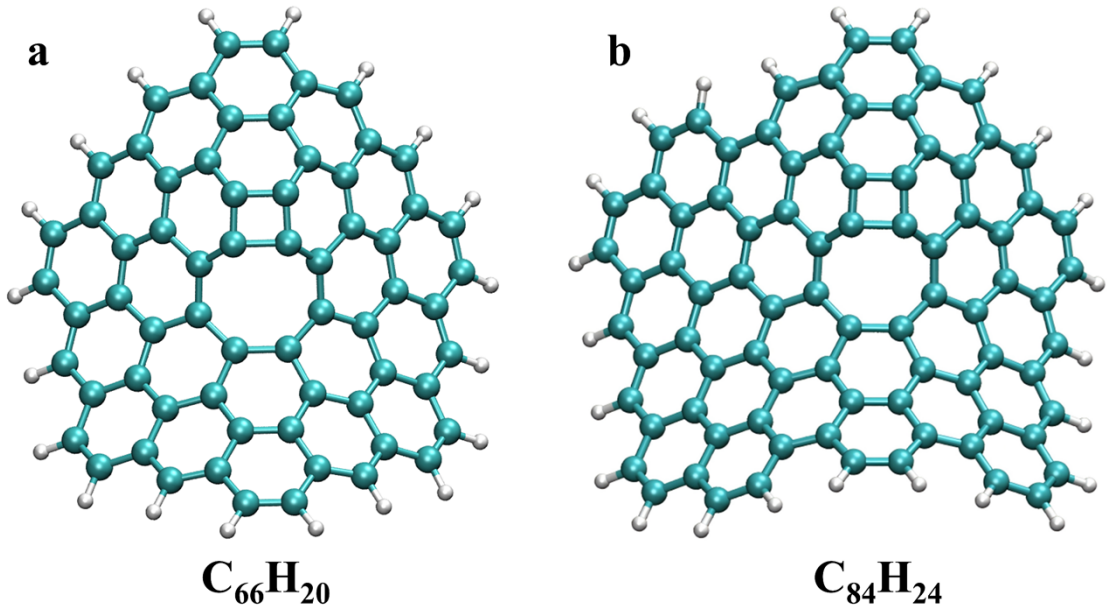

Fig. S1 Structural models of graphene clusters with different sizes: $C_{66}H_{20}$(a) and $C_{84}H_{24}$(b). The colors of atoms were as follows: C: cyan; H: white.

For the 4-C configuration, the average C-C bond length changes only slightly from 1.453 Å in $C_{66}H_{20}$ to 1.448 Å in $C_{84}H_{24}$, while the Pt-C distance decreases from 2.08 to 2.05 Å. The adsorption energy changes from -24.7 to -25.3 kcal/mol, corresponding to a difference of only 0.6 kcal/mol. The Mulliken charge of Pt remains essentially unchanged (0.040 vs 0.039 e). Similarly, for the 8-C configuration, the average C-C bond length changes from 1.458 to 1.464 Å, and the Pt-C distance changes only from 2.12 to 2.11 Å. The adsorption energy varies slightly from -13.8 to -14.1 kcal/mol, with a difference of 0.3 kcal/mol, while the Pt charge remains nearly identical (about −0.01 e in both models).

These results indicate that enlarging the graphene cluster does not lead to any substantial change in the local coordination environment, electronic characteristics, or Pt anchoring strength around the defect sites. Therefore, although the finite cluster models show some structural relaxation, the smaller $C_{66}H_{20}$ model is sufficient to capture the essential local interaction features of the graphene-supported Pt site. Considering the significantly reduced computational cost, the $C_{66}H_{20}$ model was

adopted in the main calculations.

Table S1 Comparison of structural and electronic parameters for Pt adsorbed on two graphene cluster models ($C_{66}H_{20}$ and $C_{84}H_{24}$) at the 4-C and 8-C sites.

Model	Site	$R_{(C-C)}$ /Å	$Q_{(C)}$ /e	$R_{(C-Pt)}$ / Å	$Q_{(Pt)}$ /e	E_{ads}(kcal/mol)
$C_{66}H_{20}$	4-C	1.453	-0.0755	2.08	0.04	-24.7
	8-C	1.458	-0.0745	2.12	-0.01	-13.8
$C_{84}H_{24}$	4-C	1.448	-0.0389	2.05	0.039	-25.3
	8-C	1.464	-0.0402	2.11	-0.01	-14.1

PS3: The spin state of various system

To ensure a consistent description of the electronic ground states for all systems considered in this work, several spin multiplicities were tested for the isolated Pt atom, graphene defect models, and their corresponding Pt-supported structures. The total energies as a function of spin multiplicity are summarized in Fig. S2, and the resulting ground-state multiplicities are listed in Table S2.

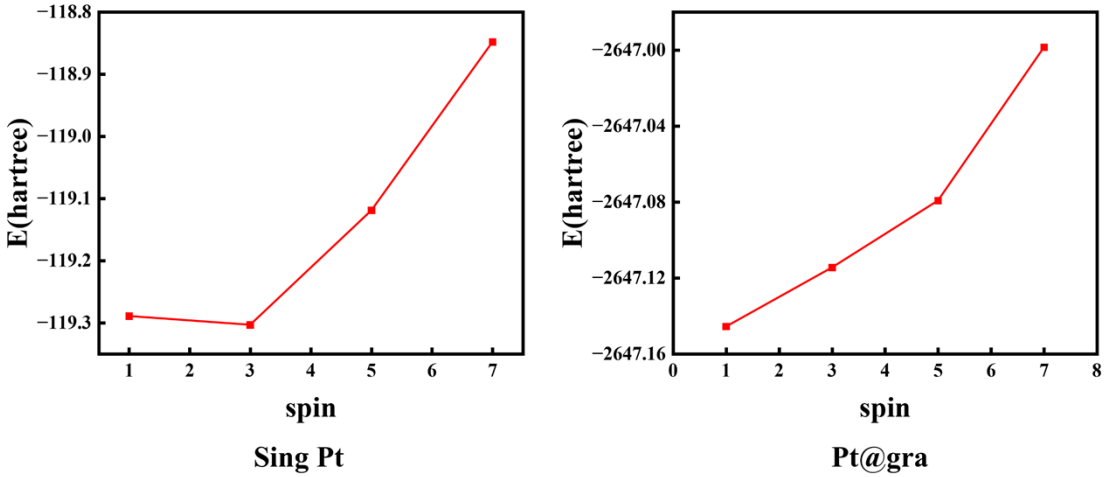

Fig. S2 Total energy as a function of spin multiplicity for a single Pt atom and the Pt@gra complex.

As shown in Fig. S2, the isolated Pt atom exhibits its lowest energy at the triplet state (spin multiplicity = 3). In contrast, the Pt@graphene complex clearly favors the singlet state (spin multiplicity = 1). For all graphene-based defect models considered in this work, including pristine graphene, 4-carbon ring, 5-carbon ring, 7-carbon ring, 8-carbon ring, 484-4-carbon ring, and 484-8-carbon ring structures, the lowest-energy state was consistently found to be the singlet for both the bare defect models and the corresponding Pt-supported complexes.

Table S2 Summary of ground-state spin multiplicities for graphene defect models and

their Pt@defect complexes.

Carbon structure	Defect spin	Pt@defect spin
Single Pt	3	-
gra	1	1
4-carbon ring	1	1
5-carbon ring	1	1
7-carbon ring	1	1
8-carbon ring	1	1
484-4-carbon ring	1	1
484-8-carbon ring	1	1

These results indicate that Pt adsorption on graphene-based supports substantially modifies the preferred spin state relative to the isolated Pt atom. Therefore, all optimized structures, adsorption energies, and reaction pathways discussed in the main text were calculated on the basis of the validated ground-state spin multiplicities, ensuring a consistent comparison among different defect environments.

PS4: Geometric parameters and charge distribution of Pt anchored on pristine

and defective graphene.

Table S3 Structural parameters and charges of defective graphene Pt single atom catalyst.

Carbon structure	$R_{(Pt-C)}$/Å	$R_{(C-C)}$/Å	$Q_{(Pt)}$/e
gra	2.15	1.46	0.00
4-carbon ring	2.08	1.50	0.04
5-carbon ring	2.13	1.45	0.02
7-carbon ring	2.13	1.56	0.03
8-carbon ring	2.12	1.63	-0.01

PS5: The most stable structure of H_2O adsorption on various Pt-loaded defective

graphene surfaces.

The most stable adsorption configurations of H_2O on different Pt-supported graphene models are shown in Fig. S3. For comparison, the O-H bond length in free H_2O is 0.96 Å. After adsorption on an isolated Pt atom, the two O-H bond lengths are both 0.97 Å, indicating only a slight change relative to the free molecule. For H_2O adsorbed on Pt@gra, the two O-H bond lengths are 0.97 and 1.01 Å. Similar structural features are also observed for the defective graphene-supported Pt systems. Specifically, the O-H bond lengths are 0.97 and 1.01 Å for Pt@gra-5-C, 0.97 and 1.01 Å for Pt@gra-7-C, and 0.97 and 1.02 Å for Pt@gra-8-C. Compared with free H_2O, one of the O-H bonds is elongated in all supported systems, suggesting that the adsorbed H_2O molecule is activated to different extents on these Pt-supported graphene structures.

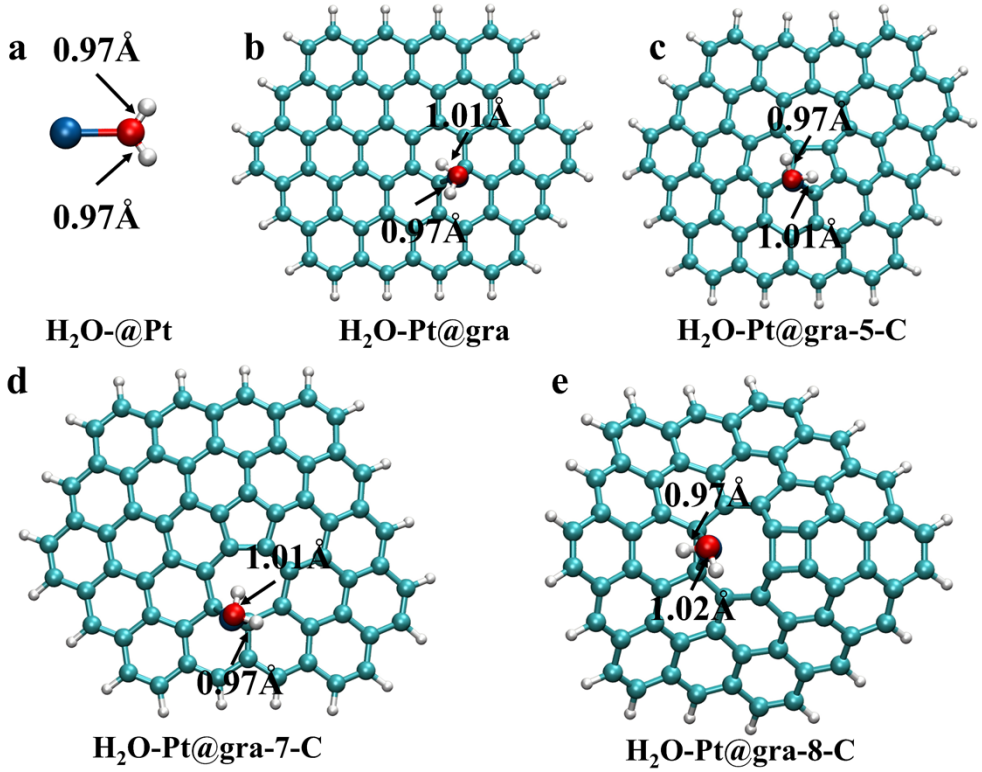

Fig. S3 Optimized adsorption configurations of H_2O on isolated Pt and Pt-supported graphene models. (a) Single atom Pt catalyst; (b) Pristine graphene Pt catalyst; (c) 5-carbon ring defect Pt catalyst; (d) 7-carbon ring defect Pt catalyst; (e) 8-carbon ring defect Pt catalyst. The colors of atoms are as follows: C: cyan; H: white; O: red; Pt: blue.

PS6: Reaction pathway for H_2O dissociation on various Pt-loaded defective graphene systems.

As shown in Fig. S4, the H_2O dissociation pathways differ among the examined defect sites. For the isolated Pt system, the dissociated •OH and •H species remain stabilized near the Pt atom, and the process releases 14.4 kcal/mol of energy. In contrast, for Pt@gra, Pt@5-C, and Pt@7-C, although the dissociated •OH and •H species are also located near the Pt atom, the corresponding dissociation processes are endothermic by 3.6, 4.8, and 3.8 kcal/mol, respectively. Different from these systems, in Pt@8-C the dissociated •OH species remains near the Pt atom, while the •H is adsorbed on the four-membered ring defect, and the process is exothermic by 11.2 kcal/mol.

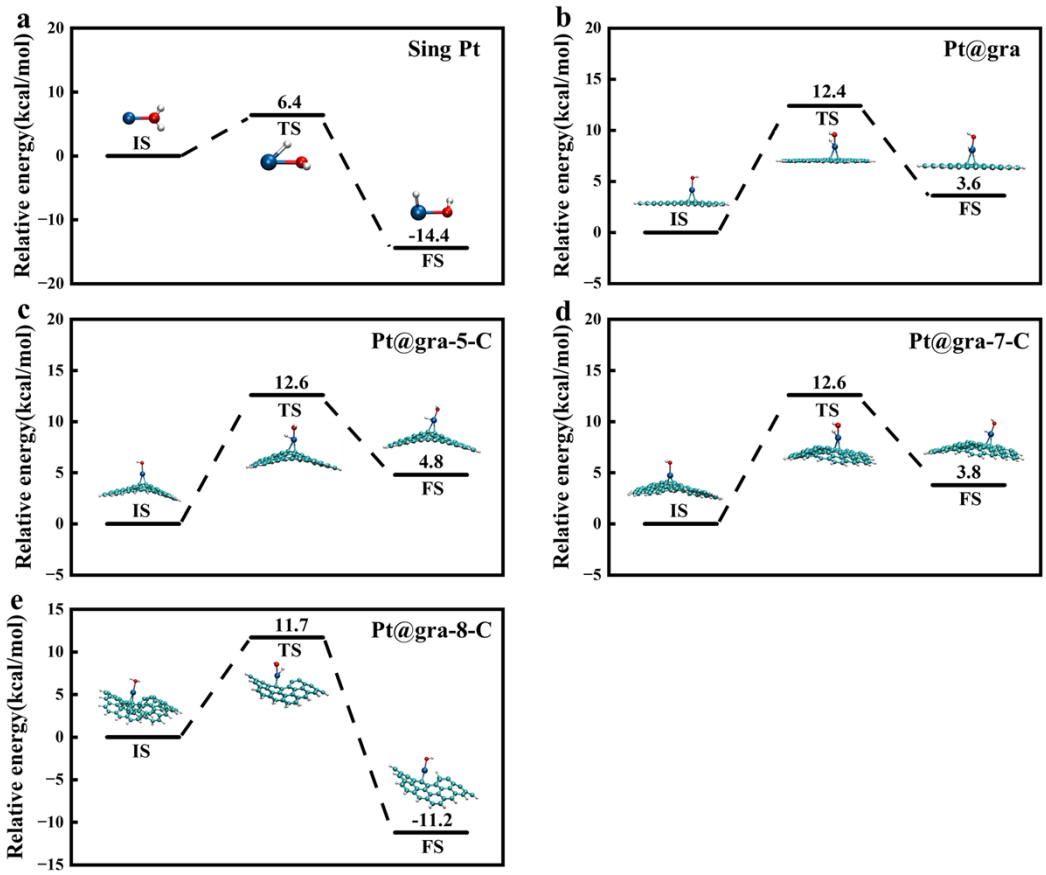

Fig S4 Reaction pathways and energy profiles for H_2O dissociation on different Pt-based systems. (a) Single atom Pt catalyst; (b) Pristine graphene Pt catalyst; (c) 5-carbon ring defect Pt catalyst; (d) 7-carbon ring defect Pt catalyst; (e) 8-carbon ring defect Pt catalyst. The colors of atoms are as follows: C: cyan; H: white; O: red; Pt: blue.

References

1 G. Shi, Y. Dang, T. Pan, X. Liu, H. Liu, S. Li, L. Zhang, H. Zhao, S. Li, J. Han, Phys. Rev. Lett. 2016, **117**, 238102.

2 G. Shi, L. Chen, Y. Yang, D. Li, Z. Qian, S. Liang, L. Yan, L.H. Li, M. Wu, H. Fang, Nat. Chem. 2018, **10**, 776–779.

3 J. Chen, X. Liu, Z. Ding, Z. He, H. Jiang, K. Zhu, Y. Li, G. Shi, Nano Lett. 2023, **23**, 10884–10891.

4 J. Shen, A. Aljarb, Y. Cai, X. Liu, J. Min, Y. Wang, Q. Wang, C. Zhang, C. Chen, M. Hakami, Science. 2025, **387**, 776–782.

5 D. Yue, T. Zeng, Y. Li, J. Lin, J. Xiao, X. Liu, Y. Ma, M. Zhu, T. Ding, Z. Liu, Phys. Rev. Lett. 2025, **135**, 038001.

6 Z. Zhang, Z. He, K. Li, J. Liu, X. Liu, Y. Luo, T. Ding, Z. Liu, X. Ye, G. Shi, Nano Lett. 2025, **25**, 2334–2341.

7 C. Paduani, Chem. Phys. 2013, **417**, 1–7.

8 B. Wu, H. Meng, X. Chen, Y. Guo, L. Jiang, X. Shi, J. Zhu, J. Long, W. Gao, F. Zeng, Angew. Chem. 2025, **137**, e202415071.

9 G.-S. Shi, Z.-G. Wang, J.-J. Zhao, J. Hu, H.-P. Fang, Chinese Physics B. 2011, **20**, 068101.

10 G. Shi, Y. Ding, H. Fang, J. Comput. Chem. 2012, **33**, 1328–1337.

11 G. Shi, J. Liu, C. Wang, B. Song, Y. Tu, J. Hu, H. Fang, Scientific reports. 2013, **3**, 3436.

12 G. Shi, Y. Shen, J. Liu, C. Wang, Y. Wang, B. Song, J. Hu, H. Fang, Scientific reports. 2014, **4**, 6793.

13 L. Chen, G. Shi, J. Shen, B. Peng, B. Zhang, Y. Wang, F. Bian, J. Wang, D. Li, Z. Qian, Nature. 2017, **550**, 380–383.

14 Y. Yang, L. Mu, L. Chen, G. Shi, H. Fang, Phys. Chem. Chem. Phys. 2019, **21**, 7623–7629.

15 X. Liu, G. Shi, Chinese Physics B. 2021, **30**, 046801.

16 L. Mu, Y. Yang, J. Liu, W. Du, J. Chen, G. Shi, H. Fang, Phys. Chem. Chem. Phys.

2021, **23**, 14662–14670.

17 F. Xiaozhen, L. Xing, H. Zhenglin, Z. Kaiyuan, S. Guosheng, J. Mol. Model. 2022, **28**, 225.

18 J. Li, X. Fan, J. Chen, G. Shi, X. Liu, J. Mol. Model. 2024, **30**, 72.

19 M. Frisch, G. Trucks, H. Schlegel, G. Scuseria, M. Robb, J. Cheeseman, G. Scalmani, V. Barone, G. Petersson, H. Nakatsuji, Wallingford, CT. 2016.